



LAWRENCE  
LIVERMORE  
NATIONAL  
LABORATORY

# Chemical and mechanical properties of carbonated wellbore cement using a multi-analytical approach

H. E. Mason, W. L. DuFrane, Z. Dai, S.  
Charnvanichborikarn, S. A. Carroll

October 3, 2012

Environmental Science and Technology

## **Disclaimer**

---

This document was prepared as an account of work sponsored by an agency of the United States government. Neither the United States government nor Lawrence Livermore National Security, LLC, nor any of their employees makes any warranty, expressed or implied, or assumes any legal liability or responsibility for the accuracy, completeness, or usefulness of any information, apparatus, product, or process disclosed, or represents that its use would not infringe privately owned rights. Reference herein to any specific commercial product, process, or service by trade name, trademark, manufacturer, or otherwise does not necessarily constitute or imply its endorsement, recommendation, or favoring by the United States government or Lawrence Livermore National Security, LLC. The views and opinions of authors expressed herein do not necessarily state or reflect those of the United States government or Lawrence Livermore National Security, LLC, and shall not be used for advertising or product endorsement purposes.

# Chemical and mechanical properties of carbonated wellbore cement using a multi-analytical approach

*Harris E. Mason<sup>1\*</sup>, Wyatt L. Du Frane<sup>1</sup>, Zurong Dai<sup>1</sup>, Supakit Charnvanichborikarn<sup>1</sup>, Susan A. Carroll<sup>1</sup>*

AUTHOR ADDRESS: <sup>1</sup>Physical and Life Sciences Directorate, Lawrence Livermore National Laboratory, 7000 East Ave. Livermore, CA 94551

AUTHOR EMAIL: mason42@llnl.gov

TITLE RUNNING HEAD: Chemical and mechanical properties of carbonated wellbore cement

## ABSTRACT

Defining chemical and mechanical alteration of wellbore cement by CO<sub>2</sub>-rich brines is important for the predicting long-term integrity of wellbores in geologic CO<sub>2</sub> environments. We reacted CO<sub>2</sub>-rich brines along cement caprock boundary at 60°C and pCO<sub>2</sub> = 3 MPa. The results show that large, distinct reaction zones form in response to reactions with the brine over the 8-day experiment. Detailed characterization of the crystalline and amorphous phases and the solution chemistry show that the zones can be modeled as preferential dissolution of portlandite in the depleted layer, concurrent alteration of calcium silicate hydrate (CSH) to an amorphous zeolite and Ca-carbonate precipitation in the carbonate layer, and carbonate dissolution in the amorphous layer. Chemical reaction altered the metrical properties of the core in which average Young's moduli in the depleted, carbonate, and amorphous layers are about 75, 64, and 34 % of the unaltered cement, respectively. The increased compressibility reflects an increase in pore space through mineral dissolution and different moduli of the reaction products.

## INTRODUCTION

Successful implementation of geologic CO<sub>2</sub> storage in deep saline and depleted oil reservoirs hinges on the long-term integrity of wellbore cements used to isolate gas and fluid flow between geologic strata, because these wells are potential sources for leakage out of the storage reservoir.<sup>1</sup> Cement is highly reactive in carbon sequestration environments in which pH and chemical gradients develop across the cement sample creating distinct reaction fronts.<sup>2-4</sup> It is unclear what the impact of the alteration is on the long-term integrity of the cement in the wellbore environment. Alteration of the cement does not necessarily lead to enhanced permeability and leakage. A recent experimental study shows a mixed response of permeability over time when reacted with acidic fluids.<sup>5</sup> The apparent reduction in permeability due to cement carbonation has also been seen in the field. Detailed analysis of wellbore cement from a CO<sub>2</sub> enhanced oil recovery field indicated some leakage along surfaces adjacent to caprock and casing, but the overall performance of the cement to isolate reservoir fluids was not compromised.<sup>6</sup> These observations suggest a strong interplay between cement carbonation and its mechanical response to *in situ* stress within the wellbore environment. Alteration of Portland cement by acids (used to accelerate degradation at ambient conditions) can significantly reduce the effective moduli making the reacted material significantly more compressible.<sup>7,8</sup> It is likely that cement carbonation and the development of distinct reaction zones will also induce structural and mechanical changes that will impact transport of gas and fluid. Ultimately, long-term assessment of wellbore performance to isolate CO<sub>2</sub> reservoir fluids will use advanced models that couple chemical, mechanical and transport processes to represent the range of

relevant parameters in the field that cannot be fully captured by experiment. Experiments can be used to defining key processes and parameters that form the basis of the advanced simulations.

The objective of this work was to two-fold: (1) to provide a cement carbonation model that ties reaction pathway to the metrical response of the alteration zones based on new data collected from a fracture flow experiment; and (2) to discuss the implications of these findings to wellbore performance in carbon storage environments. We collected a detailed, spatially resolved dataset to constrain the reaction pathways and structural changes occurring during the carbonation of wellbore cements. Cement carbonation reactions were identified from solid-state nuclear magnetic resonance (NMR) spectroscopic analyses, scanning electron microscopy (SEM), powder X-ray diffraction (XRD) and solution chemistry. Chemically induced geomechanical changes were identified by spatially resolved nanoindentation and macroscopic loading measurements.

## METHODS

### *Reaction of wellbore cement with CO<sub>2</sub> saturated brine*

We reacted cured Class G Portland cement with CO<sub>2</sub> saturated brine in two different flow-through systems to generate samples representative of CO<sub>2</sub> leakage in the wellbore environment. Class G Portland cement used was cured in brine using a hydrothermal vessel in accordance with ASTM Test Method C114. The core flood experiment followed the procedures outlined by Smith et al.<sup>10</sup>, and used a sample core (15 mm diameter, 37 mm length) that was half cement - half caprock with a planar fracture between the two materials. A fracture pathway between the two flat surfaces was generated by abrading the cement surface with glass beads prior to joining the two halves. The core was maintained at a confining pressure of 24.8 MPa and 60 °C. Brine was maintained at 60 °C in a separate pressure vessel and saturated with either 0 or

3 MPa partial pressure  $\text{CO}_2$  ( $p\text{CO}_2$ ). Brine was injected through a hastelloy frit into the core with an average flow rate of  $0.05 \text{ cm}^3/\text{min}$  with pore pressure fixed to 12.4 MPa at the outlet by a back pressure regulator. The core was equilibrated with  $\text{CO}_2$  free brine for 7 days prior to reaction with brine that contained  $p\text{CO}_2 = 3 \text{ MPa}$  for an additional 7 days. Pressure conditions were varied in the first and last days of reaction to test the geomechanical response of the sample core. *In situ* measurements of the inlet pressure ( $P_{\text{inlet}}$ ) and outlet pressure ( $P_{\text{outlet}}$ ) were used to calculate differential pressure across the sample ( $\Delta P = P_{\text{inlet}} - P_{\text{outlet}}$ ) and pore pressure ( $P_{\text{pore}} = \Delta P / 2$ ). Reacted output brine was periodically sampled and aliquots submitted for total inorganic carbon (TIC), inductively coupled plasma mass spectrometry (ICP-MS) and ion chromatography (IC) analyses. Speciation calculations were made from the measured solution chemistry with EQ3 and the ymp thermodynamic data in which solution pH was calculated from charge balance.<sup>11</sup> After reaction, a total of nine subsamples of the reacted cement half core were taken using careful grinding of the core with fine tweezers and steel rasp. The weights of the resulting powders were recorded and samples were analyzed by powder X-ray diffraction (XRD) from  $10^\circ$  to  $50^\circ 2\theta$  using a Bruker D8 Advance X-ray diffractometer, and solid-state NMR spectroscopy.

We also conducted a flow through experiment<sup>12</sup> to react a larger volume of cement for use in additional NMR experiments requiring more material. The brine was maintained in a separate mixer pressure vessel at  $60^\circ \text{C}$  with  $p\text{CO}_2 = 3 \text{ MPa}$ . The cement was equilibrated for 24 hours with  $\text{CO}_2$ -free brine before the  $\text{CO}_2$  saturated brine was injected through the inlet of the reactor vessel at a rate of  $0.10 \text{ cm}^3/\text{min}$  for 7 days, with total pressure fixed at 6.5-7.0 MPa by back-pressure regulator at the outlet.

*Nanoindentation*

Measurements were performed at room temperature with an MTS XP Nanoindenter with a diamond Berkovich indenter tip in load control mode. Maximum loads of 10, 25, 50, 125, 250, and 250 mN were used. Partial load-unload data were analyzed with the Oliver-Pharr method to calculate the hardness and elastic modulus as a function of indenter penetration.<sup>13</sup> Maximum displacements between 4-10  $\mu\text{m}$  were selected in order to probe larger volumes to minimize effects of the heterogeneous phase distribution in the reacted cement. Measurements were made in a transect across the sample to capture the properties in each alteration layer.

#### *SEM Analysis*

The same polished sample section was gold coated and analyzed with scanning electron microscopy (SEM) and X-ray energy dispersive spectroscopy (EDS). These analyses were performed at 20 kV under a FEI Inspect F scanning electron microscope equipped with an Everhart-Thornley secondary-electron detector, a solid state diode backscattered-electron detector and an EDAX APOLLO XL X-ray detector with energy resolution better than 133 eV at Mn-K and an active area of 30 mm<sup>2</sup>. Segmentation of SEM images was done with a user guided seeded region growing method.<sup>14</sup>

#### *Solid-state NMR spectroscopy*

The <sup>29</sup>Si single-pulse magic angle spinning (SP/MAS) NMR spectra of the reacted cement subsamples were collected on a Bruker Avance 400 spectrometer using a double resonance Doty Scientific probe configured for 4 mm (o.d.) rotors. Typical spectra were collected at a spinning rate of 7 kHz using an 8 s pulse delay for 8 000 – 20 000 acquisitions each. Additional <sup>29</sup>Si SP/MAS and <sup>29</sup>Si{<sup>1</sup>H} cross polarization (CP) MAS spectra were collected for samples from the flow through experiment using a Doty Scientific probe configured for 7 mm (o.d.) rotors. The <sup>27</sup>Al SP/NMR spectra were collected on a Bruker AMX 500 spectrometer

using a triple resonance Doty Scientific probe configured for 4 mm (o.d.) rotors. Each spectrum was collected at a spinning rate of 12.5 kHz using a 0.2 s pulse delay for 36 864 acquisitions to ensure spectral intensities are directly comparable among sample spectra. The  $^{27}\text{Al}\{^1\text{H}\}$  rotational echo double resonance (REDOR) experiments were conducted on the 400 spectrometer using a Bruker HXY probe configured for 4 mm (o.d.) diameter rotors. The  $^1\text{H}$  NMR spectra were collected at a spinning rate of 55 kHz on a 600 MHz Bruker Avance III spectrometer using a Bruker Very Fast MAS probe configured for 1.3 mm (o.d) diameter rotors using a background suppression pulse sequence.<sup>15</sup> The  $^{29}\text{Si}$  and  $^1\text{H}$  NMR spectra were referenced with respect to an external standard of TMS ( $\delta_{\text{Si,H}} = 0$  ppm) and the  $^{27}\text{Al}$  spectra were referenced with respect to 0.1 M  $\text{AlCl}_3$  solution ( $\delta_{\text{Al}} = 0$  ppm)

## RESULTS AND DISCUSSION

### *Spatially resolved analysis of wellbore cement carbonation*

The reactions of the cement with  $\text{CO}_2$  saturated brine produce three distinct alteration zones parallel to the initial cement – caprock interface that can be clearly observed by SEM analysis of the core flood sample (Figure 1). These regions are similar to those previously described by Kutchko and coworkers.<sup>2-4</sup> Accordingly, we will adopt a similar naming scheme when discussing these layers throughout this study. The first layer (red in Figure 1B) will be referred to as the amorphous layer and has an average thickness of 930  $\mu\text{m}$ , the second (blue in Figure 1B) is the carbonate layer and averages 190  $\mu\text{m}$  thick, and the final layer (green in Figure 1B) is the depleted region and has an average thickness of 650  $\mu\text{m}$ . The remainder of the core is unaltered cement. The alteration layers and their average thicknesses have been defined using image segmentation methods. The total extent of reaction in this sample is  $\sim 2$  mm, and is on



average thicker than those observed previously.<sup>2-4</sup> The remainder of the 7 mm diameter core appears unaffected by carbonation reactions and is denoted as unaltered cement.

Further information about the reactions that occur in these layers can be gained from sequential sampling and analysis of these layers as a function of reaction depth. The XRD results provide information about how the crystalline phases in these samples are changing (Figure 2). The unreacted cement contains portlandite,  $\text{Ca}_3\text{SiO}_5$  (alite;  $\text{C}_3\text{S}$ ) and the calcium aluminate phase brownmillerite ( $\text{C}_4\text{AF}$ ) as the dominant crystalline phases (Figure 2a). As the reaction progresses we observe distinct layers that are marked by disappearance of portlandite and  $\text{C}_3\text{S}$  (Figure 2d), the emergence of calcite and aragonite (Figure 2d-f), and finally the dissolution of these carbonate phases (Figure 2g). The final layer contains only residual peaks from calcite and  $\text{C}_4\text{AF}$ .

Given that the majority of the minerals present in hardened Portland cement are poorly crystalline or amorphous,<sup>9</sup> the XRD results alone cannot fully trace all the reactions occurring in this system. We used  $^{29}\text{Si}$  and  $^{27}\text{Al}$  NMR spectroscopy to provide information on the alteration of these phases (Figure 3). The  $^{29}\text{Si}$  NMR data supplies information about the  $\text{C}_3\text{S}$  and amorphous calcium silicate hydrate (CSH) phases, which represent the majority of the cement. The peak at -74 ppm arises from residual  $\text{C}_3\text{S}$  clinker material and the two peaks at -82 and -87 ppm result from the  $\text{Q}^1$  and  $\text{Q}^2$  silica sites in the CSH phase, respectively (Figure 3a). We observe that in the least reacted regions (Figure 3a-b; as indicated by SEM and XRD) there is little change in the collected NMR spectra. However, as the reaction fronts progress we see a rapid loss of structure beginning at the edge of the carbonate zone (Figure 3c) and a complete loss of structure through the carbonate layer (Figure 3d) and into the amorphous layer (Figure 3e). Comparison of the

XRD and NMR suggests that the Ca-leaching of the CSH occurs simultaneously with the formation of calcium carbonate formation.

As the alteration of the cement progresses, the Al environment changes from being dominated by octahedrally coordinated Al (Al<sup>[6]</sup>; Figure 3f) to tetrahedrally coordinated Al (Al<sup>[4]</sup>; Figure 3j). Minor amounts of Al<sup>[4]</sup> observed in the least reacted samples (Figure 3f) likely represent Al in CSH minerals.<sup>16, 17</sup> The major change observed indicates a shift from a Al<sup>[6]</sup> dominant phase such as an oxide or sulfate to a Al<sup>[4]</sup> dominant phase such as an aluminosilicate. The Al<sup>[6]</sup> is likely contained in Al-sulfate phases,<sup>18</sup> since Al<sup>[6]</sup> in Ca-ferrite phases cannot be observed in <sup>27</sup>Al NMR experiments due to their high Fe content.<sup>19</sup> The increase in the Al signal intensity of the spectra collected for the amorphous layers (Figure 3j) likely occurs from the dissolution of Fe-rich phases and incorporation of Al into silicate phases.

#### *Geomechanical characterization*

Geochemical alteration by CO<sub>2</sub>-saturated brine significantly weakened the cement. The differential pressure data (ΔP) was used to make a parallel plate approximation of hydraulic aperture (b):

$$b = \left( \frac{12Q\mu l}{\Delta P w} \right)^{\frac{1}{3}} \quad (1)$$

where  $Q$  is flow rate,  $\mu$  is the temperature-dependent dynamic viscosity of the brine,  $l$  is the core length,  $w$  is the core diameter.<sup>20</sup> The hydraulic aperture reduced by a factor of ~3, and was more sensitive to changes in normal stress after the alteration (Figure 4).

The individual hardness and Young's moduli values measured across the reaction zones by nanoindentation exhibit a large degree of scatter that reflects the heterogeneity at the micron scale within each layer (Figure 5). The average values for hardness agree with those reported previously for reaction zones in carbonated cement (Figure 5A).<sup>4</sup> The average Young's moduli

decreased across the reaction zones from  $28 \pm 7$  GPa in the unaltered cement to  $21 \pm 6$  GPa in the depleted layer, to  $18 \pm 3$  GPa in the carbonate layer, and finally to  $9.6 \pm 1.0$  GPa in the amorphous layer (Figure 5B). The final layer lies closest to the fracture surface and exhibits significantly less compressive strength than the others. The SEM and EDS (not shown) analyses of the depleted layer suggest that mostly CSH grains were sampled by nanoindentation, and the observed weakening is likely due to increased porosity from mineral dissolution. Ultrasonic measurements on two pristine cement cores and compressive load testing on third core measured an average Young's modulus of 19 GPa that is lower than that obtained by nanoindentation for the unreacted layer. This disparity may indicate that the strength of the cement constituents is greater than the bulk values observed by macroscopic methods or that continued curing during the experiment slightly strengthened this layer. The nanoindentation measurements were performed on a dry sample, and the presence of H<sub>2</sub>O could alter the mechanical values, particularly for the amorphous layer which would have been weaker in the wet sample.<sup>21</sup>

#### *Characterization of the amorphous cement layer*

It has been largely assumed that the end product of the carbonation reactions with CSH is amorphous silica based largely on mass balance calculations. We employed additional NMR measurements to identify the major mineral constituent of the amorphous layer as an amorphous aluminosilicate. This result is reasonable since Mg-aluminosilicates have been previously found to replace Ca-silicate grains in naturally altered cement.<sup>22, 23</sup>

Important information about phase identity can be gleaned from the hydration state. We gathered such information from <sup>1</sup>H SP/MAS, <sup>27</sup>Al{<sup>1</sup>H} REDOR and <sup>29</sup>Si{<sup>1</sup>H} CP/MAS NMR measurements of the amorphous layer. First, we observed that the <sup>1</sup>H NMR spectrum collected at 55 kHz produces only a single peak at 4.8 ppm with a strong sideband pattern characteristic of

structural water molecules (not shown).<sup>24</sup> Absent were peaks from structural hydroxyls that occur between 0 ppm and 2 ppm.<sup>24</sup>  $^{29}\text{Si}\{^1\text{H}\}$  CP/MAS NMR can be used to enhance the observed  $^{29}\text{Si}$  signal from  $^1\text{H}$  polarization transfer from abundant silanol protons.<sup>25</sup> However, we observed a significant decreases in the intensity of the  $^{29}\text{Si}\{^1\text{H}\}$  CP/MAS spectra when compared to SP/MAS spectra (not shown) that indicates that either only a small subset of silanol groups exist or more likely that the polarization transfer from structural waters is inefficient at enhancing the observed signal. These observations are supported by the  $^{27}\text{Al}\{^1\text{H}\}$  REDOR experiment which can be used to constrain the identity of aluminosilicate phases.<sup>26</sup> We measured a REDOR dephasing curve for the amorphous layer that is similar to the zeolite phase mordenite which contains mobile structural waters (Figure 6). The mobility of the water quenches the dipole coupling and explains both the decrease in the REDOR dephasing and the decreased signal intensity for the  $^{29}\text{Si}\{^1\text{H}\}$  CP/MAS NMR spectrum.

Geochemical speciation calculations of the output solution chemistry were consistent with the above solid analysis. Geochemical alteration buffers more acid input  $\text{CO}_2$ -rich input solution from pH 4.3 to pH  $5.08 \pm 0.08$  and yields output solutions that were in equilibrium with calcite ( $\log\text{SI } 0.05 \pm 0.11$ ), anhydrite ( $\log\text{SI } -0.07 \pm 0.02$ ), mordenite ( $\log\text{SI } -0.22 \pm 0.16$ ) and quartz ( $\log\text{SI } 0.11 \pm 0.02$ ). Saturation indices were calculated from 5 to 144 hours (Figure 7). The equilibrium assemblage between calcite, mordenite, and quartz may be suggestive of rapid diffusion of reactants and products through the amorphous layer, or it may simply reflect equilibrium within the fracture zone between quartz and calcite in the caprock and mordenite in the amorphous layer. The final sample was slightly more acidic (pH 4.9) and undersaturated with respect the calcite, mordenite, and quartz assemblage.

If the cement samples were allowed to dry that shrinkage cracks would develop in the amorphous layer that coated the reacted samples (c.f. Figure 1). These features could develop through the loss of structural water in the amorphous aluminosilicate or through loss of pore water. The loss of structural water could substantially change the structure of the amorphous material, and manifest as distinct changes in the  $^{29}\text{Si}$  NMR spectra. We, therefore, collected  $^{29}\text{Si}$  spectra of flow through samples immediately after the experiment was brought down when the layer was still wet, and after the sample had been dried in a  $50^\circ\text{C}$  oven overnight. We observe no changes in the spectra of these samples, and conclude the shrinkage cracks do not result from substantive structural changes, but rather the loss of pore water. This conclusion is supported by a prior study that attributed such features to expulsion of water from the amorphous layer via syneresis.<sup>27</sup>

Based on the above results, we assign the majority amorphous component to an amorphous aluminosilicate of similar composition to the zeolite minerals mordenite or clinoptilolite. The difference between these two minerals is largely structural. We cannot differentiate between the two with the current analytical methods, nor is it appropriate to assign a specific crystalline structure since this material is amorphous and by definition lacks long range structural order. However, this phase is metastable and could be expected to transform to a thermodynamic endmember.

#### *Revised geochemical pathways*

Previous models suggest these layers form first through the dissolution of portlandite, followed by the precipitation of Ca-carbonate, and finally the leaching of Ca from silicates to form amorphous silica after the Ca-carbonates have dissolved.<sup>2,3</sup> The largest differences in our model compared to that previously proposed is that alteration of CSH occurs concurrently with

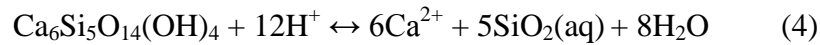
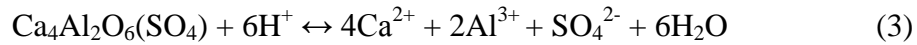
Ca-carbonate precipitation and that the final alteration phase is an amorphous zeolite and not amorphous silica. We will discuss the proposed cement alteration reactions in detail as they relate to the three discrete reaction zones observed (Figure 8).

At the boundary of the unaltered and depleted zones, pH gradients produced from carbonation reactions cause portlandite to dissolve and initially supply dissolved  $\text{Ca}^{2+}$  to the system, without significant precipitation of Ca-carbonate.



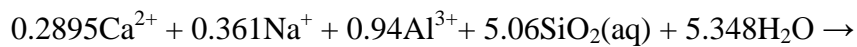
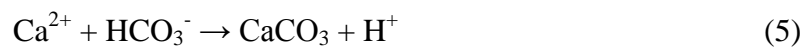
Any alteration of the CSH in the depleted layer appears to be negligible based on the absence of the amorphous aluminosilicate reaction product as detected by NMR.

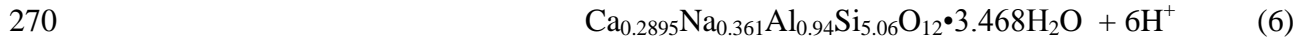
At the boundary of the carbonate and depleted zones, the presence of carbonic acid triggers a series of linked reactions causing calcium-aluminum-monosulfate and CSH to dissolve.



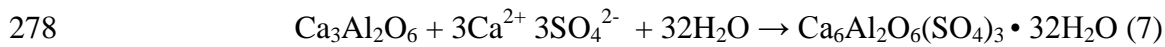
The composition of the CSH phase has a Ca:Si ratio of 1.2 and approximates the general chemical formula used above based on a detailed study of well-defined CSH phases that correlates  $\text{Q}^1:\text{Q}^2$  abundances to Ca:Si ratios.<sup>28</sup> The water content in the mass balance equations is difficult to constrain because it is not possible to obtain the structural water content of the CSH within the current heterogeneous cement sample using the current analytical methods.

The dissolution reactions (3 and 4) result in calcite, aragonite, and amorphous aluminosilicate precipitation:

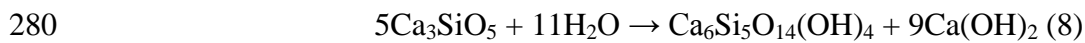




271 The leaching of Ca from CSH phases consumes  $\text{Na}^+$  from the brine and the dissolved  $\text{Al}^{3+}$  to  
 272 form an amorphous zeolite modeled here as mordenite. Mechanistically we do not know if  
 273 alteration of CSH to zeolite occurs through dissolution and precipitation as described above, or  
 274 through structural reorientation caused by the diffusion of Na and Al for Ca. In either case, the  
 275 reaction can be modeled with equations 2 – 6. The completion of the above reactions also results  
 276 in the hydration of residual anhydrous clinker materials. Ca-aluminates react with water and  
 277 available sulfate sources to form additional Ca-Al-sulfates to feed dissolution reactions.



279 Anhydrous  $\text{C}_3\text{S}$  reacts with water to form additional CSH phases for the leaching reactions.



281 These reactions produce complex feedback loops, which continue until the clinker materials have  
 282 been fully consumed by the carbonation reactions.

283 At the final boundary between the carbonate and amorphous zones, Ca-carbonate phases  
 284 dissolve due to strong pH gradients from the  $\text{CO}_2$ -rich brine. Ca-carbonate dissolution results in  
 285 a substantial amount of pore space that is taken up by water.

286 The reactions involving Al are important given the influence that even small amounts of  
 287 Al can have on the precipitation and dissolution of silicate minerals,<sup>29-31</sup> but have been largely  
 288 overlooked in carbonation reactions. The  $^{27}\text{Al}$  NMR data showing that carbonation induces a  
 289 change from  $\text{Al}^{[6]}$  sulfate minerals to  $\text{Al}^{[4]}$  silicate minerals. This finding is counter to prior  
 290 assumptions that Al should partition into  $\text{Al}^{[6]}$ -oxides/hydroxides.<sup>9</sup> The feedback loop proposed  
 291 is supported by the  $^{27}\text{Al}$  spectra collected for the amorphous layer, which show a large increase  
 292 in the spectral intensity relative to the unreacted layers. This data suggests that previously

“invisible” Al has dissolved from the Fe-rich Ca-aluminate phases and partitions into the amorphous aluminosilicates.

There are two significant differences between our results and from those of previous studies of wellbore cement carbonation. Most notably, we observe the development of larger reaction zones (~2 mm) over a shorter experimental duration (8 days). Studies by Kutchko et al presented the results of batch alteration experiments where small (500  $\mu\text{m}$ ) reaction zones emerged after 9 days of reaction.<sup>2,3</sup> Similarly, work by Carey et al observed only 50 to 150  $\mu\text{m}$  of alteration after 16.6 days of reaction.<sup>32</sup> The more extensive reaction zones observed in our experiments may reflect difference in design where the brine is continually replaced and does not have the potential to reach equilibrium with the carbonation products as it could in a batch setup. Geochemical modeling of cement alteration indicates sensitivities to not only the brine chemistry and initial mineralogical composition of the cements, but also physical parameters such as tortuosity and permeability.<sup>33</sup>

The geochemical model presented above attempts to more completely capture all the reactions which occur during cement alteration. In addition to added reaction pathways, it significantly modifies the existing models for the transport of Ca in the system. In the model of Kutchko et al<sup>2,3</sup>, the formation of the Ca-carbonate layer was understood to protect the Ca-silicate materials from leaching reactions, and leaching only occurred after these carbonate minerals were dissolved. Our analytical results suggest that Ca-leaching is concurrent with the formation of Ca-carbonate minerals. The alteration of the silicates is evidenced by the loss of distinct peaks for CSH and C<sub>3</sub>S in the <sup>29</sup>Si NMR spectra (Figure 3d) as well as the absence of C<sub>3</sub>S peaks in XRD patterns (Figure 2d-f) collected for carbonate layer subsamples. Backscattered



SEM images also show substantial amounts of dark grains with similar morphology to the silicate grains within this carbonate zone that result from the loss of Ca (Figure 9).

#### *Implications for wellbore stability*

We have identified key geochemical reactions and geomechanical properties for the alteration layers that result from cement carbonation. This data can provide the basis for coupled chemical – mechanical – flow models<sup>33</sup> to evaluate the long term stability of wellbores used in CO<sub>2</sub> sequestration activities. Our combined dataset suggest that carbonation may seal potential fractures between the caprock and cemented sections of the wellbore. The development of such large reaction fronts over a short period of time would seem detrimental to the long-term stability of the wellbore, and counter to findings which show some wellbore cement seals to be stable during CO<sub>2</sub> injection for decades.<sup>6</sup> However, the geochemical alteration of these layers produce a more compressible material which under the confining pressures of the wellbore could be expected to self-seal. This conclusion is consistent with our macroscopic mechanical measurements that show a three-fold decrease in the hydraulic aperture from the beginning to the end of the experiment. The findings of this study provide valuable input to predictive models, but further constraints on changes in parameters such as porosity, tortuosity, and effective diffusivity are required to adequately address the influence of wellbore cement carbonation on carbon sequestration activities.

#### ACKNOWLEDGEMENTS

This work was funded by the DOE, Office of Fossil Fuel, National Risk Assessment Project. We would like to thank M. Smith for assistance with the initial setup of the core-flood experiment, S. Walsh for input on the paper, S. Torres and D. Ruddle for preparation of sample cores, L. Knauer

and the California Well Sample Repository for the caprock samples, D. Urabe for load testing, K. Fisher for ultrasonic testing, V. Genetti and R. Lindvall for IPCMS measurement, and S. Kucheyev for assistance with nanoindentation measurements. This work was performed by LLNL under Contract DE-AC52-07NA27344

## REFERENCES

1. Watson, T. L.; Bachu, S., Evaluation of the Potential for Gas and CO<sub>2</sub> Leakage Along Wellbores. *Spe Drilling & Completion* **2009**, *24*, (1).
2. Kutchko, B. G.; Strazisar, B. R.; Dzombak, D. A.; Lowry, G. V.; Thaulow, N., Degradation of well cement by CO<sub>2</sub> under geologic sequestration conditions. *Environmental Science & Technology* **2007**, *41*, (13), 4787-4792.
3. Kutchko, B. G.; Strazisar, B. R.; Lowry, G. V.; Dzombak, D. A.; Thaulow, N., Rate of CO<sub>2</sub> attack on hydrated Class H well cement under geologic sequestration conditions. *Environmental Science & Technology* **2008**, *42*, (16), 6237-6242.
4. Kutchko, B. G.; Strazisar, B. R.; Huerta, N.; Lowry, G. V.; Dzombak, D. A.; Thaulow, N., CO<sub>2</sub> Reaction with Hydrated Class H Well Cement under Geologic Sequestration Conditions: Effects of Flyash Admixtures. *Environmental Science & Technology* **2009**, *43*, (10), 3947-3952.
5. Huerta, N. J.; Hesse, M. A.; Bryant, S. L.; Strazisar, B. R.; Lopano, C. L., Experimental Evidence for Self-Limiting Reactive Flow through a Fractured Cement Core: Implications for Time-Dependent Wellbore Leakage. *Environmental Science & Technology* **2012**.
6. Carey, J. W.; Wigand, M.; Chipera, S. J.; WoldeGabriel, G.; Pawar, R.; Lichtner, P. C.; Wehner, S. C.; Raines, M. A.; Guthrie, G. D., Jr., Analysis and performance of oil well cement with 30 years Of CO<sub>2</sub> exposure from the SACROC Unit, West Texas, USA. *International Journal of Greenhouse Gas Control* **2007**, *1*, (1), 75-85.
7. Constantinides, G.; Ulm, F.; Van Vliet, K., On the use of nanoindentation for cementitious materials. *Materials and Structures* **2003**, *36*, (257).
8. Ulm, F. J., Chemomechanics of concrete at finer scales. *Materials and Structures* **2003**, *36*, (261).
9. Zhang, M.; Bachu, S., Review of integrity of existing wells in relation to CO<sub>2</sub> geological storage: What do we know? *International Journal of Greenhouse Gas Control* **2011**, *5*, (4), 826-840.
10. Smith, M. M.; Sholokhova, Y.; Hao, Y.; Carroll, S., Evaporite Caprock Integrity: An experimental study of reactive mineralogy and pore-scale heterogeneity during brine-CO<sub>2</sub> exposure. *Environmental Science & Technology* **2012**.
11. Wolery, T. W. *EQ3/6, a software package for geochemical modeling of aqueous systems.*; Lawrence Livermore National Laboratory: Livermore, CA, 1992.
12. Carroll, S. A.; Knauss, K. G., Dependence of labradorite dissolution kinetics on CO<sub>2</sub>(aq), Al(aq), and temperature. *Chemical Geology* **2005**, *217*, (3-4).
13. Oliver, W. C.; Pharr, G. M., An improved technique for determining hardness and elastic-modulus using load and displacement sensing indentation experiments. *Journal of Materials Research* **1992**, *7*, (6).

14. Schindelin, J.; Arganda-Carreras, I.; Frise, E.; Kaynig, V.; Longair, M.; Pietzsch, T.; Preibisch, S.; Rueden, C.; Saalfeld, S.; Schmid, B.; Tinevez, J. Y.; White, D. J.; Hartenstein, V.; Eliceiri, K.; Tomancak, P.; Cardona, A., Fiji: an open-source platform for biological-image analysis. *Nature Methods* **2012**, 9, (7), 676-682.
15. Cory, D. G.; Ritchey, W. M., Suppression of signals from the probe in Bloch decay spectra. *Journal of Magnetic Resonance* **1988**, 80, (1), 128-132.
16. Andersen, M. D.; Jakobsen, H. J.; Skibsted, J., Incorporation of aluminum in the calcium silicate hydrate (C-S-H) of hydrated Portland cements: A high-field  $^{27}\text{Al}$  and  $^{29}\text{Si}$  MAS NMR Investigation. *Inorganic Chemistry* **2003**, 42, (7), 2280-2287.
17. Houston, J. R.; Maxwell, R. S.; Carroll, S. A., Transformation of meta-stable calcium silicate hydrates to tobermorite: reaction kinetics and molecular structure from XRD and NMR spectroscopy. *Geochemical Transactions* **2009**, 10.
18. Skibsted, J.; Henderson, E.; Jakobsen, H. J., Characterization of calcium aluminate phases in cement by  $^{27}\text{Al}$  MAS NMR spectroscopy. *Inorganic Chemistry* **1993**, 32, (6), 1013-1027.
19. Skibsted, J.; Jakobsen, H. J.; Hall, C., Quantitative aspects of  $^{27}\text{Al}$  MAS NMR of calcium aluminoferrites. *Advanced Cement Based Materials* **1998**, 7, (2), 57-59.
20. Polak, A.; Elsworth, D.; Yasuhara, H.; Grader, A. S.; Halleck, P. M., Permeability reduction of a natural fracture under net dissolution by hydrothermal fluids. *Geophysical Research Letters* **2003**, 30, (20).
21. Smith, D. M.; Scherer, G. W.; Anderson, J. M., Shrinkage during drying of silica-gel. *Journal of Non-Crystalline Solids* **1995**, 188, (3).
22. Scherer, G. W.; Kutchko, B.; Thaulow, N.; Duguid, A.; Mook, B., Characterization of cement from a well at Teapot Dome Oil Field: Implications for geological sequestration. *International Journal of Greenhouse Gas Control* **2011**, 5, (1), 115-124.
23. Brown, P. W.; Doerr, A., Chemical changes in concrete due to the ingress of aggressive species. *Cement and Concrete Research* **2000**, 30, (3), 411-418.
24. Yesinowski, J. P.; Eckert, H.; Rossman, G. R., Characterization of hydrous species in minerals by high-speed  $^1\text{H}$  MAS NMR. *Journal of the American Chemical Society* **1988**, 110, (5), 1367-1375.
25. Liu, C. H. C.; Maciel, G. E., The fumed silica surface: A study by NMR. *Journal of the American Chemical Society* **1996**, 118, (21), 5103-5119.
26. Mason, H. E.; Maxwell, R. S.; Carroll, S. A., The formation of metastable aluminosilicates in the Al-Si-H<sub>2</sub>O system: Results from solution chemistry and solid-state NMR spectroscopy. *Geochimica Et Cosmochimica Acta* **2011**, 75, (20), 6080-6093.
27. Matteo, E. N.; Scherer, G. W., Experimental study of the diffusion-controlled acid degradation of Class H Portland cement. *International Journal of Greenhouse Gas Control* **2012**, 7, 181-191.
28. Cong, X. D.; Kirkpatrick, R. J.,  $^{29}\text{Si}$  MAS NMR study of the structure of calcium silicate hydrate. *Advanced Cement Based Materials* **1996**, 3, (3-4), 144-156.
29. Van Cappellen, P.; Dixit, S.; van Beusekom, J., Biogenic silica dissolution in the oceans: Reconciling experimental and field-based dissolution rates. *Global Biogeochemical Cycles* **2002**, 16, (4).
30. Carroll, S.; Mroczek, E.; Alai, M.; Ebert, M., Amorphous silica precipitation (60 to 120 degrees C): Comparison of laboratory and field rates. *Geochimica Et Cosmochimica Acta* **1998**, 62, (8), 1379-1396.

- 426 31. Bickmore, B. R.; Nagy, K. L.; Gray, A. K.; Brinkerhoff, A. R., The effect of  $\text{Al}(\text{OH})_4^-$  on  
427 the dissolution rate of quartz. *Geochimica Et Cosmochimica Acta* **2006**, 70, (2), 290-305.
- 428 32. Carey, J. W.; Svec, R.; Grigg, R.; Lichtner, P. C.; Zhang, J.; Crow, W., Wellbore  
429 integrity and  $\text{CO}_2$ -brine flow along the casing-cement microannulus. *Greenhouse Gas Control*  
430 *Technologies* 9 **2009**, 1, (1).
- 431 33. Walsh, S. D. C.; Du Frane, W. L.; Mason, H. E.; Carroll, S. A., Permeability of wellbore-  
432 cement fractures following degradation by carbonated brines. *Rock Mechanics and Rock*  
433 *Engineering* **2012**, submitted.
- 434
- 435

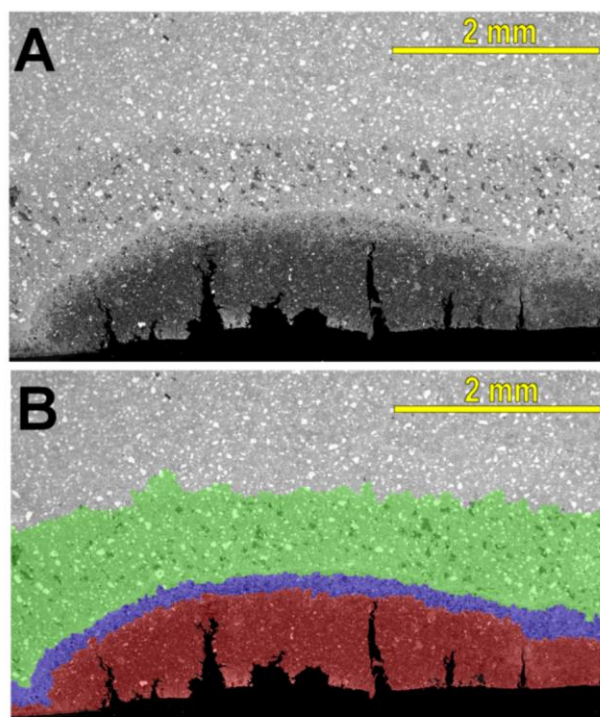


Figure 1

437  
438 **Figure 1.** Backscattered SEM images of the core flood sample. **A.** Original SEM image. **B.** The  
439 results of image segmentation are presented as colored overlays on the original image to  
440 highlight the reaction zones. Red: Amorphous layer. Blue: Carbonate layer. Green: Depleted  
441 layer.

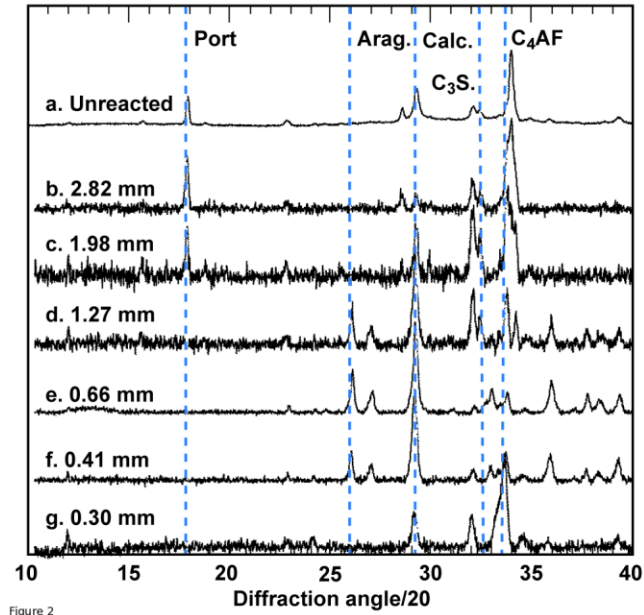


Figure 2

**Figure 2.** Powder X-ray diffraction patterns for **a.** unreacted cement and **b-f.** sequentially sampled sections of CFE cement sample. Measurements in mm are given for the depth of sampling from the fracture surface.

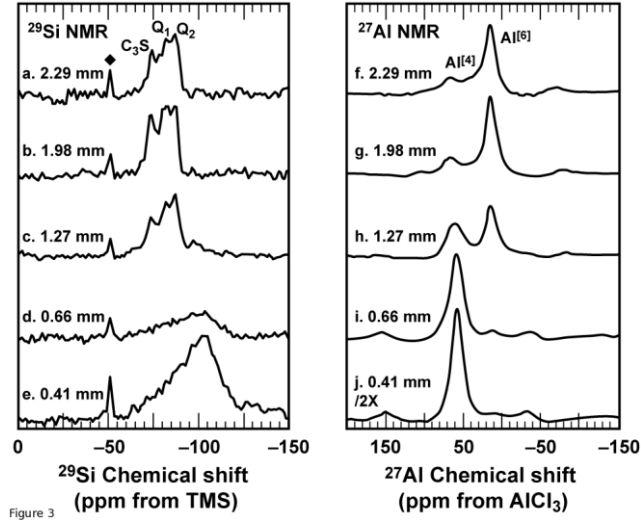
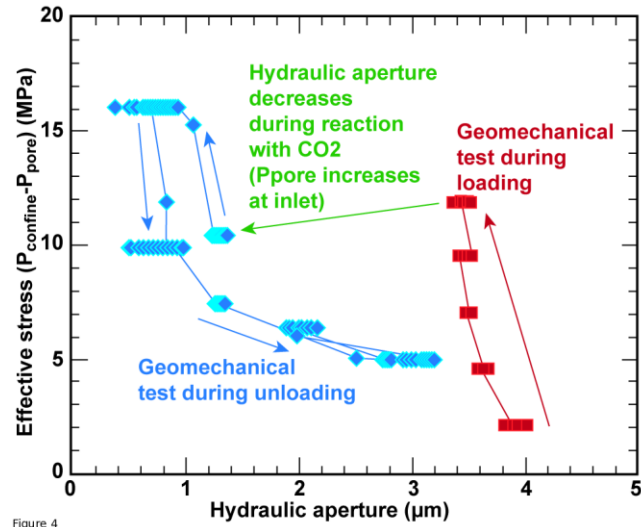


Figure 3

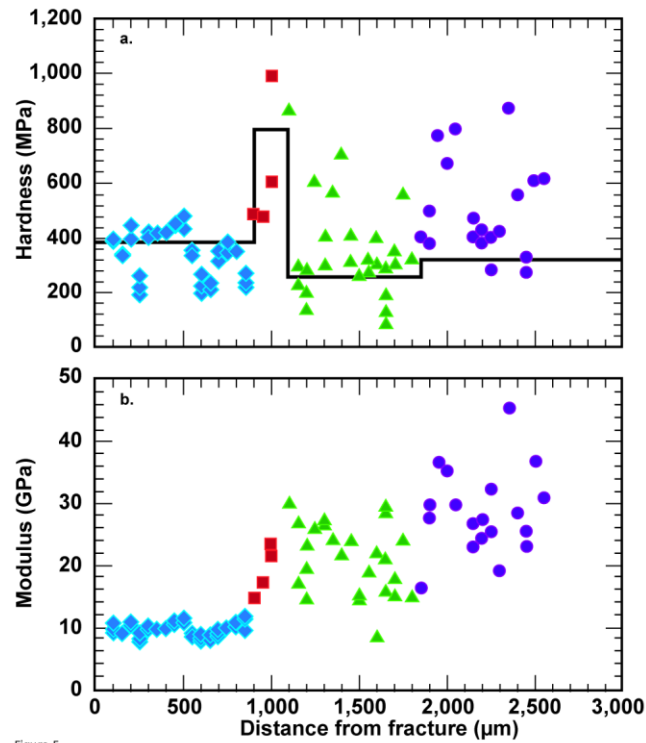
**Figure 3.** Stacked NMR plots of sequentially sampled cement from the CFE. Left:  $^{29}\text{Si}$  NMR spectra. **a.** Peaks associated with  $\text{C}_3\text{S}$  and  $\text{Q}^1$  and  $\text{Q}^2$  peaks of CSH are labeled and diamond identifies background peak from SiN rotor. Right:  $^{27}\text{Al}$  NMR spectra. **f.** Peaks identified are identified as occurring from  $\text{Al}^{[4]}$  and  $\text{Al}^{[6]}$ . Bottom  $^{27}\text{Al}$  NMR spectrum is downscaled by a factor of 2X



**Figure 4.** Changes to hydraulic aperture in response to changes in effective pressure on fracture before (red squared and line) and after cement reaction with brine containing CO<sub>2</sub> (blue diamonds and line).



457  
458



459

460 **Figure 5.** Nanoindentation measurements on CFE sample of **a.** Young's modulus and **B)**  
461 hardness in transect across each reaction zone: amorphous (blue diamonds), carbonate (red  
462 squares), depleted cement (green triangles), and unreacted cement (purple circles). **b.** Hardness  
463 measurements for these layers in experiments by Kutchko et al.<sup>4</sup> and average ultrasonic, load  
464 measurements of Young's modulus (19 GPa, this study) of unreacted cement are plotted as grey  
465 lines for comparison.

466

467

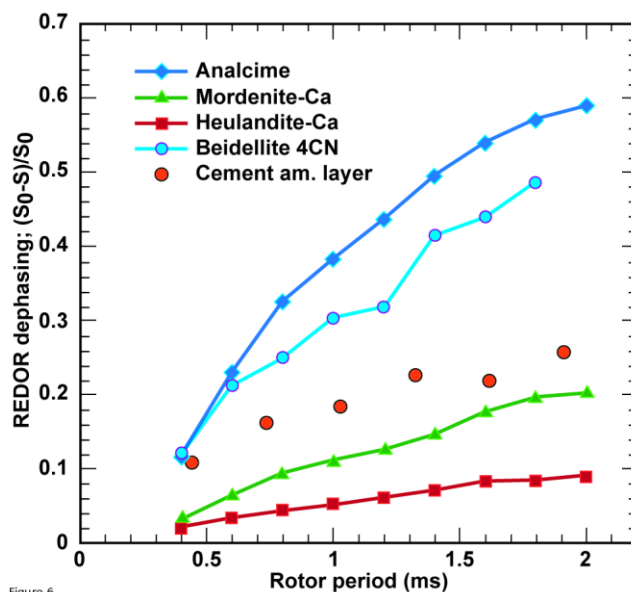


Figure 6

468

469 **Figure 6.**  $^{27}\text{Al}\{^1\text{H}\}$  REDOR NMR results for various aluminosilicate minerals and the  
 470 amorphous cement layer. Since beidellite contains both  $^{[6]}\text{Al}$  and  $^{[4]}\text{Al}$ , only the results for  $^{[4]}\text{Al}$   
 471 peak are presented. Lines are present only to guide the eye.

472

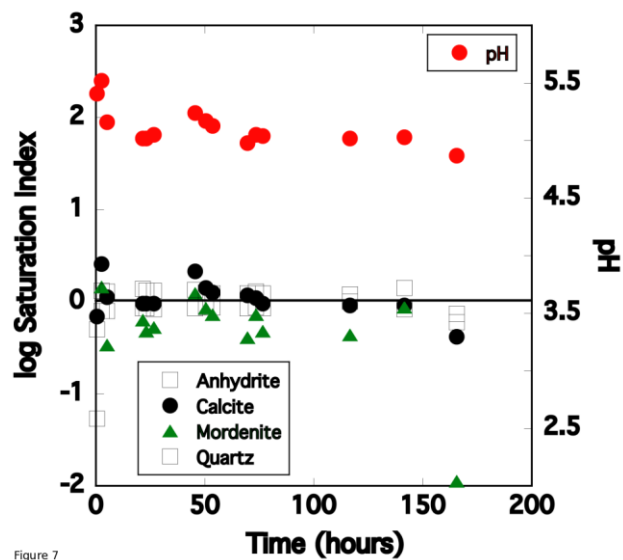
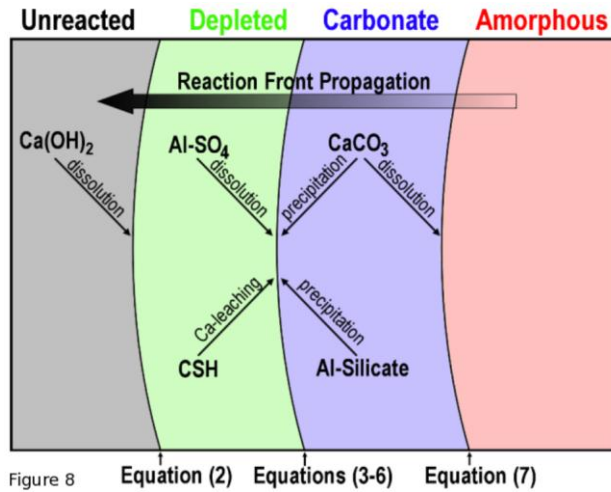


Figure 7

**Figure 7.** Output solution pH, and mineral saturations plotted as log SI vs time for Analcime, Mordenite, Anhydrite, Calcite and Quartz. Averaged values reported in the main manuscript reflect steady-state values averaged after 23 hours of reaction.



**Figure 8.** Schematic representation of the main reactions and their location with respect to the development of the alteration zones. The equations refer to those which occur at the reaction front and are detailed in the text.

484

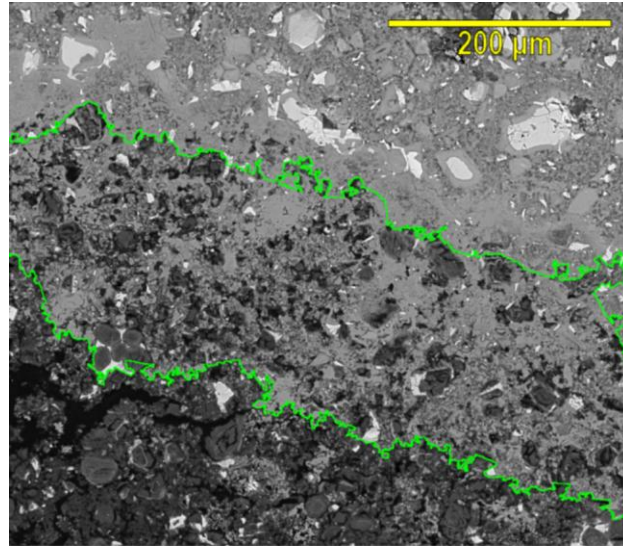


Figure 9

485

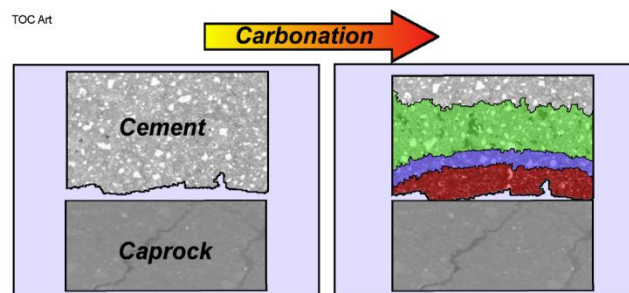
486 **Figure 9.** Backscattered SEM Image of the core flood sample showing the transitions from the  
487 amorphous to carbonate to depleted zones. Green lines mark the layer boundaries as determined  
488 by image segmentation. Pervasive dark grains can be observed throughout the carbonate layer..

489

490

491

492 TOC ART



493

494

495

496